To appear in the *International Journal of Pavement Engineering*
Vol. 00, No. 00, 00 Month 20XX, 1–20

A thermodynamically compatible model for describing asphalt binders: Solutions of problems

J. Málek[a], K. R. Rajagopal[c*] and K. Tůma[ab]

[a] *Charles University in Prague, Faculty of Mathematics and Physics, Mathematical Institute of Charles University, Sokolovská 83, 186 75 Prague 8, Czech Republic*
[b] *Institute of Fundamental Technological Research, Polish Academy of Sciences, Adolfa Pawińskiego 5B, 02-106 Warsaw, Poland*
[c] *Texas A&M University, Department of Mechanical Engineering, College Station, TX 77843, USA*

(*November 2014*)

In this sequel to the first paper (Málek et al. (2014)), in which we identified a generalization of the model due to Burgers which was corroborated against two sets of experiments, including a challenging one showing distinctly different relaxation times for shear and normal stresses, we solve several time dependent boundary value problems wherein the boundary of the material is deforming, that have relevance to applications involving asphalt. Problems wherein the boundary is subject to time varying compressive loads such as those due to moving automobiles and the attendant rutting, and the compaction due to rollers are considered in additions to other problems.

Keywords: Rate type fluid; asphalt; finite element method; monolithic ALE method

1. Introduction

In Málek *et al.* (2014) we put into place a thermodynamically compatible rate type fluid model, that is a generalization of the model due to Burgers, to describe the response of asphalt binders. The model was validated against two sets of experiments. The first set of experiments carried out by Narayan *et al.* (2012) concerned the relaxation of the shear and normal forces in a torsional experiment which provided a very challenging set of data in that the relaxation times associated with the normal and shear stresses differed by an order of magnitude. The model that was developed was able to explain this phenomenon quite well while the currently used models in the field are unable to do so. The second set of experiments concerned the stress overshoot observed by Krishnan and Narayan (2007) which once again currently used models are unable to describe. Once again, the model that was developed by Málek *et al.* (2014) was able to describe the data exceedingly well. Having validated the model against these two sets of demanding experiments we feel it meaningful to use it to study more complicated initial-boundary value problems. We start with a study to describe the secondary flow observed in the experiment of Narayan *et al.* (2012). We follow this up with the study of the problem of rutting and the problem of compaction due to rolling.

In this study we shall not repeat the development of the models but plunge in straight away to document the model and discuss the various problems that are considered. The organization of the paper is as follows: After introducing the model derived by Málek *et al.* (2014) we compute the simulation of the torsional experiment performed by Narayan *et al.* (2012) including the

*Corresponding author. Email: krajagopal@tamu.edu

full set of partial differential equations with appropriate boundary and initial conditions. We compare the results with those obtained by Málek *et al.* (2014) where several assumptions are used in order to obtain the set of ordinary differential equations that can be solved quickly and is amenable to fitting the material parameters. This is followed by our consideration of problems wherein the domain as well as the boundary are deforming. We reformulate the problem within the context of an arbitrary Lagrangian-Eulerian description as such a description is better suited for flows occurring in deformable domains. We compute four evolutionary problems in two space dimensions. The first problem that we study is a simple problem that is meant to introduce the readers to the salient features of the model. In this problem, the material is at rest and initial time $t = 0$, a normal traction is applied to a part of the boundary and is held for a time interval and then the traction is removed (see Figure 6). The subsequent deformation of the body is observed. This is followed by a more realistic problem wherein the boundary traction is applied over a portion of the boundary and the subsequent deformation of the domain is studied. The third problem corresponds to the problem of rutting wherein we apply time varying boundary tractions on two disjoint pieces of the boundary corresponding to where a tire would contact a pavement (see Figure 11). The last problem is the simulation of the rolling of the asphalt. We conclude with a brief discussion of the results.

2. Non-linear incompressible viscoelastic rate type fluid model – non-linear Burgers model

The non-linear incompressible viscoelastic rate type fluid model derived by Málek *et al.* (2014) using two natural configurations (see also Rajagopal and Srinivasa (2004) and Krishnan and Rajagopal (2005)) is presented here. It is a non-linear version of Burgers model and it will be used for the simulation of all problems

$$\operatorname{div} \mathbf{v} = 0\,, \tag{1a}$$

$$\rho \dot{\mathbf{v}} = \operatorname{div} \mathbf{T}\,, \tag{1b}$$

$$\mathbf{T} = -p\mathbf{I} + 2\nu\mathbf{D} + \mu_1 \mathbf{B}^d_{\kappa_{p_1(t)}} + \mu_2 \mathbf{B}^d_{\kappa_{p_2(t)}}\,, \tag{1c}$$

$$\overset{\triangledown}{\mathbf{B}}_{\kappa_{p_1(t)}} = -\frac{1}{\tau_1}\mathbf{B}_{\kappa_{p_1(t)}}\mathbf{B}^d_{\kappa_{p_1(t)}}\,, \tag{1d}$$

$$\overset{\triangledown}{\mathbf{B}}_{\kappa_{p_2(t)}} = -\frac{1}{\tau_2}\mathbf{B}_{\kappa_{p_2(t)}}\mathbf{B}^d_{\kappa_{p_2(t)}}\,, \tag{1e}$$

where ν is the viscosity, μ_1 and μ_2 are the elastic shear moduli, τ_1, τ_2 are the relaxation times[1], $\mathbf{v}$ is the fluid velocity, ρ is the density, $\mathbf{T}$ is the Cauchy stress, p is the pressure, $\mathbf{B}_{\kappa_{p_1(t)}}$ and $\mathbf{B}_{\kappa_{p_2(t)}}$ are extra stress tensors, $\mathbf{D} = (\nabla\mathbf{v} + (\nabla\mathbf{v})^{\mathrm{T}})/2$ is the symmetric part of velocity gradient. $\overset{\triangledown}{\mathbf{A}}$ denotes the upper convected Oldroyd derivative

$$\overset{\triangledown}{\mathbf{A}} = \frac{\partial \mathbf{A}}{\partial t} + \mathbf{v}\cdot\nabla\mathbf{A} - (\nabla\mathbf{v})\mathbf{A} - \mathbf{A}(\nabla\mathbf{v})^{\mathrm{T}}. \tag{2}$$

$\mathbf{A}^d$ denotes the deviatoric part of the tensor $\mathbf{A}$

$$\mathbf{A}^d = \mathbf{A} - \frac{1}{3}(\operatorname{tr}\mathbf{A})\mathbf{I} \text{ in 3D}, \quad \mathbf{A}^d = \mathbf{A} - \frac{1}{2}(\operatorname{tr}\mathbf{A})\mathbf{I} \text{ in 2D}. \tag{3}$$

[1]Here the relaxation times τ_1 and τ_2 are used instead of the ratios $\epsilon_1/(2\mu_1)$ and $\epsilon_2/(2\mu_2)$ that were used in paper by Málek *et al.* (2014).

In all problems that are computed within the paper, the material is at $t = 0$ at rest with the following initial conditions:

$$p(0) = 0, \quad \mathbf{v}(0) = \mathbf{0}, \quad \mathbf{B}_{\kappa_{p_1(t)}}(0) = \mathbf{B}_{\kappa_{p_2(t)}}(0) = \mathbf{I}. \tag{4}$$

We can observe one interesting property of the model (1). If the relaxation times $\tau_1 = \tau_2 = \tau$ are equal and $\mathbf{B}_{\kappa_{p_1(t)}}$ and $\mathbf{B}_{\kappa_{p_2(t)}}$ satisfy the same initial conditions then the model reduces to the model derived by Málek *et al.* (2014) using one natural configuration

$$\operatorname{div} \mathbf{v} = 0\,, \tag{5a}$$

$$\rho \dot{\mathbf{v}} = \operatorname{div} \mathbf{T}\,, \tag{5b}$$

$$\mathbf{T} = -p\mathbf{I} + 2\nu \mathbf{D} + \mu \mathbf{B}_{\kappa_{p(t)}}\,, \tag{5c}$$

$$\overset{\triangledown}{\mathbf{B}}_{\kappa_{p(t)}} = -\frac{1}{\tau} \mathbf{B}_{\kappa_{p(t)}} \mathbf{B}^d_{\kappa_{p(t)}}\,, \tag{5d}$$

where $\mu = \mu_1 + \mu_2$.

3. Simulations

3.1 *Full simulation of the experiment performed by Narayan et al. (2012)*

We briefly describe the experiment performed by Narayan *et al.* (2012) that is simulated here. The torsional rheometer consists of two plates, the lower one is fixed and does not move, the upper one can rotate, the radius of the plates was $R = 4$ mm. A sample of asphalt binder was placed between the plates and it was squeezed to a thickness of $h = 1$ mm. Finally, at time $t = 0$ the upper plate was set into motion with an angular velocity 0.5 rad s^{-1} and at $t = 0.5$ s its rotation was stopped and the corresponding torque and normal force was recorded up to the time $t = 2$s. The angular velocity ω is equal to

$$\omega = \begin{cases} 0.5 \text{ rad s}^{-1} & 0 \text{ s} \le t \le 0.5 \text{ s}, \\ 0 \text{ rad s}^{-1} & 0.5 \text{ s} < t \le 2.0 \text{ s}. \end{cases} \tag{6}$$

Málek *et al.* (2014) fitted this experiment under the simplifying assumptions that the asphalt flows only in the direction of rotation, i.e.

$$\mathbf{v} = (0, \omega r z/h, 0) \tag{7}$$

and neglecting the time derivative of ω. In this subsection we show the full simulation of this experiment with the material parameters for model (1) fitted by Málek *et al.* (2014) for the unaged polymer modified binder at the temperature 35°C with the density[1] $\rho = 1200$ kg/m^3:

Temp [°C]	μ_1 [kPa]	μ_2 [kPa]	τ_1 [s]	τ_2 [s]	ν [kPa s]
35	27.7	130.4	1.52	0.17	45.3

Table 1. Fitted parameters for the torque and the normal force by Málek *et al.* (2014).

We solve the full problem using the cylindrical coordinates in the fixed domain Ω_x. The only assumption that is used is that the solution does not depend on the ϕ coordinate. Such an

[1] Using the assumptions mentioned above the density is not presented in the simplified equations computed in Málek *et al.* (2014) and so was not used.

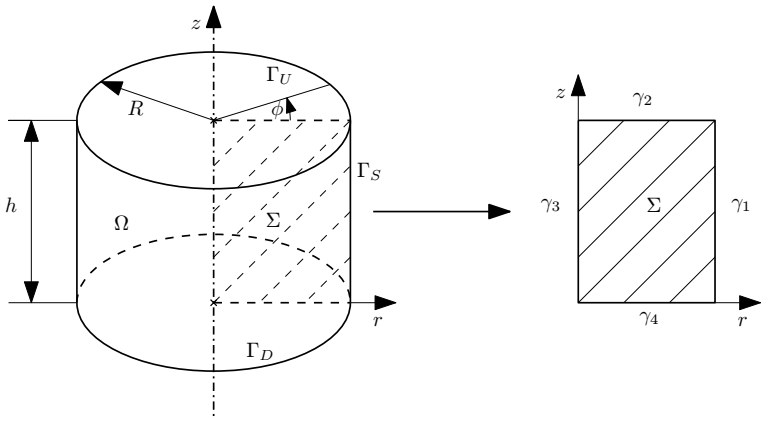

Figure 1. Cross-section Σ in cylindrical coordinates.

assumption allows us to solve the problem in the cross-section Σ, see Figure 1. The unknowns in (1) are expressed in the form

$$p = p(r,z,t),\ \mathbf{v} = (v_r, v_\phi, v_z)(r,z,t),\ \mathbf{B}_{\kappa_{p_1(t)}} = \begin{pmatrix} B_{1rr}, B_{1r\phi}, B_{1rz} \\ B_{1r\phi}, B_{1\phi\phi}, B_{1\phi z} \\ B_{1rz}, B_{1\phi z}, B_{1zz} \end{pmatrix}(r,z,t),$$

$$\mathbf{B}_{\kappa_{p_2(t)}} = \begin{pmatrix} B_{2rr}, B_{2r\phi}, B_{2rz} \\ B_{2r\phi}, B_{2\phi\phi}, B_{2\phi z} \\ B_{2rz}, B_{2\phi z}, B_{2zz} \end{pmatrix}(r,z,t), \quad (r,z) \in \Sigma,\ t \in [0,2].$$

The initial conditions are provided in (4). The boundary conditions that need to be satisfied are

$$\mathbf{Tn} = \mathbf{0} \text{ on } \gamma_1 \tag{8}$$

$$v_r = v_z = 0,\ v_\phi = \omega r \text{ on } \gamma_2 \tag{9}$$

$$v_r = v_\phi = v_z = 0 \text{ on } \gamma_4 \tag{10}$$

with symmetry boundary conditions specified on γ_3

$$v_r = v_\phi = 0, T_{rz} = 0 \text{ on } \gamma_3. \tag{11}$$

The Dirichlet conditions on γ_2, γ_3 and γ_4 are taken into account by choosing the appropriate space and the Neumann conditions on γ_1 ad γ_3 are part of the weak formulation.

For numerical implementation all computations were carried out using the weak formulation in the form

$$\int_{\Omega_x} \mathrm{tr}(\nabla \mathbf{v}) q \,\mathrm{d}x = 0, \tag{12a}$$

$$\int_{\Omega_x} \rho \left[\frac{\partial \mathbf{v}}{\partial t} + (\nabla \mathbf{v})\mathbf{v}\right] \cdot \mathbf{q} \,\mathrm{d}x - \int_{\Omega_x} \mathbf{T} \cdot \nabla \mathbf{q} \,\mathrm{d}x + \int_{\Gamma_N} \mathbf{t} \cdot \mathbf{q} \,\mathrm{d}S = 0, \tag{12b}$$

$$\mathbf{T} = -p\mathbf{I} + \nu\left((\nabla \mathbf{v}) + (\nabla \mathbf{v})^{\mathrm{T}}\right) + \mu_1 \mathbf{B}^d_{\kappa_{p_1(t)}} + \mu_2 \mathbf{B}^d_{\kappa_{p_2(t)}}, \tag{12c}$$

$$\int_{\Omega_x} \left[\frac{\partial \mathbf{B}_{\kappa_{p_1(t)}}}{\partial t} + (\nabla \mathbf{B}_{\kappa_{p_1(t)}})\mathbf{v} - (\nabla \mathbf{v})\mathbf{B}_{\kappa_{p_1(t)}} - \mathbf{B}_{\kappa_{p_1(t)}}(\nabla \mathbf{v})^{\mathrm{T}} + \frac{1}{\tau_1}\mathbf{B}_{\kappa_{p_1(t)}}\mathbf{B}^d_{\kappa_{p_1(t)}}\right] \cdot \mathbf{Q}_1 \,\mathrm{d}x = 0, \tag{12d}$$

$$\int_{\Omega_x} \left[\frac{\partial \mathbf{B}_{\kappa_{p_2(t)}}}{\partial t} + (\nabla \mathbf{B}_{\kappa_{p_2(t)}})\mathbf{v} - (\nabla \mathbf{v})\mathbf{B}_{\kappa_{p_2(t)}} - \mathbf{B}_{\kappa_{p_2(t)}}(\nabla \mathbf{v})^{\mathrm{T}} + \frac{1}{\tau_2}\mathbf{B}_{\kappa_{p_2(t)}}\mathbf{B}^d_{\kappa_{p_2(t)}}\right] \cdot \mathbf{Q}_2 \,\mathrm{d}x = 0. \tag{12e}$$

Under the assumption of axial symmetry, the weak formulation of the equations is transformed from 3D to 2D in the following way

$$\int_{\Omega_x} \operatorname{div} \mathbf{v}\ q \,\mathrm{d}\mathbf{x} = \int_0^R \int_0^h \int_0^{2\pi} r \operatorname{div} \mathbf{v}\ q \,\mathrm{d}\phi \,\mathrm{d}z \,\mathrm{d}r = \int_\Sigma r \operatorname{div} \mathbf{v} \left(\int_0^{2\pi} q \,\mathrm{d}\phi \right) \mathrm{d}\Sigma = \int_\Sigma r \operatorname{div} \mathbf{v}\ \hat{q} \,\mathrm{d}\Sigma, \tag{13}$$

where we denote by $\hat{q}$ a new 2D test function computed from the old 3D test function q

$$\hat{q}(r,z) = \int_0^{2\pi} q(r,\phi,z) \,\mathrm{d}\phi.$$

The same procedure is applied to the rest of the equations

$$\int_\Sigma r \operatorname{div} \mathbf{v}\ \hat{q}\ \mathrm{d}\Sigma = 0, \tag{14a}$$

$$\int_\Sigma \rho r \left(\frac{\partial \mathbf{v}}{\partial t} + \mathbf{v} \cdot \nabla \mathbf{v} \right) \cdot \mathbf{q}\ \mathrm{d}\Sigma + \int_\Sigma r \mathbf{T} \cdot \nabla \hat{\mathbf{q}}\ \mathrm{d}\Sigma = 0, \tag{14b}$$

$$r\mathbf{T} = -rp\mathbf{I} + r\nu \left(\nabla \mathbf{v} + (\nabla \mathbf{v})^{\mathrm{T}} \right) + rG_1 \mathbf{B}^d_{\kappa_{p_1(t)}} + rG_2 \mathbf{B}^d_{\kappa_{p_2(t)}}, \tag{14c}$$

$$\int_\Sigma r \left[\frac{\partial \mathbf{B}_{\kappa_{p_1(t)}}}{\partial t} + \mathbf{v} \cdot \nabla \mathbf{B}_{\kappa_{p_1(t)}} - (\nabla \mathbf{v}) \mathbf{B}_{\kappa_{p_1(t)}} - \mathbf{B}_{\kappa_{p_1(t)}} (\nabla \mathbf{v})^{\mathrm{T}} + \frac{1}{\tau_1} \mathbf{B}_{\kappa_{p_1(t)}} \mathbf{B}^d_{\kappa_{p_1(t)}} \right] \cdot \hat{\mathbf{Q}}_1\ \mathrm{d}\Sigma = 0, \tag{14d}$$

$$\int_\Sigma r \left[\frac{\partial \mathbf{B}_{\kappa_{p_2(t)}}}{\partial t} + \mathbf{v} \cdot \nabla \mathbf{B}_{\kappa_{p_2(t)}} - (\nabla \mathbf{v}) \mathbf{B}_{\kappa_{p_2(t)}} - \mathbf{B}_{\kappa_{p_2(t)}} (\nabla \mathbf{v})^{\mathrm{T}} + \frac{1}{\tau_2} \mathbf{B}_{\kappa_{p_2(t)}} \mathbf{B}^d_{\kappa_{p_2(t)}} \right] \cdot \hat{\mathbf{Q}}_2\ \mathrm{d}\Sigma = 0, \tag{14e}$$

where

$$\hat{\mathbf{q}}(r,z) = \int_0^{2\pi} \mathbf{q}(r,\phi,z) \,\mathrm{d}\phi, \quad \hat{\mathbf{Q}}_1(r,z) = \int_0^{2\pi} \mathbf{Q}_1(r,\phi,z) \,\mathrm{d}\phi, \quad \hat{\mathbf{Q}}_2(r,z) = \int_0^{2\pi} \mathbf{Q}_2(r,\phi,z) \,\mathrm{d}\phi \tag{15}$$

and all gradients are expressed in the cylindrical coordinates.

3.1.1 Numerical results

In order to solve the problem described by the weak formulation (14) numerically, a discrete approximation has to be created.

3.1.1.1 Time discretization. For the simulation of the experiment the discretization in time is done by two unconditionally stable schemes. Let us consider the following equation

$$\frac{\partial y(x,t)}{\partial t} = f(y(x,t)) \text{ in } \Omega_x \times [0,T], \tag{16}$$

then the time derivative is discretized by two different time schemes:

Implicit backward Euler scheme The first order unconditionally stable time scheme.

$$\frac{y^{n+1}(x) - y^n(x)}{\Delta t^n} = f(y^{n+1}(x)), \tag{17}$$

where Δt^n is the $n-$th time step, $y^{n+1}(x) = y(x, t_0 + \sum_{i=0}^n \Delta t^i)$ and on every $(n+1)$-th time level the space problem is solved.

Implicit three-step θ scheme The second order unconditionally stable time scheme (see for example Glowinski (1985)). Let us define $\theta = 1 - \sqrt{2}/2$, $\alpha = (1-2\theta)/(1-\theta)$, then the

time derivative is approximated in three steps:

$$1.\quad \frac{y^{n+\frac{1}{3}}(x)-y^n(x)}{\theta\Delta t^n}=\alpha f(y^{n+\frac{1}{3}}(x))+(1-\alpha)f(y^n(x)),$$

$$2.\quad \frac{y^{n+\frac{2}{3}}(x)-y^{n+\frac{1}{3}}(x)}{(1-2\theta)\Delta t^n}=(1-\alpha)f(y^{n+\frac{2}{3}}(x))+\alpha f(y^{n+\frac{1}{3}}(x)),$$

$$3.\quad \frac{y^{n+1}(x)-y^{n+\frac{2}{3}}(x)}{\theta\Delta t^n}=\alpha f(y^{n+1}(x))+(1-\alpha)f(y^{n+\frac{2}{3}}(x)).$$

For the simulations of the problems with deforming domains another time discretization is used. Since f in ALE (Arbitrary Lagrangian-Eulerian) formulation instead of (16) includes time derivative of u, i.e.

$$\frac{\partial y(x,t)}{\partial t}=f\left(y(x,t),\frac{\partial y(x,t)}{\partial t}\right)\ \text{in}\ \Omega_x\times[0,T], \tag{18}$$

it is not clear how for example the Crank-Nicolson time scheme or three-step θ-scheme should be implemented in the case of (18) with fully mixed time derivatives. For this purpose we use the higher order time scheme (almost third order) proposed by Glowinski (2003) and tested by Turek *et al.* (2006).

Implicit Glowinski three-step scheme This time scheme consists of two implicit Euler steps, we define $\theta := 1-1/\sqrt{2}$:

$$1.\quad \frac{y^{n+\theta}(x)-y^n(x)}{\theta\Delta t^n}=f\left(y^{n+\theta}(x),\frac{y^{n+\theta}(x)-y^n(x)}{\theta\Delta t^n}\right),$$

$$2.\quad y^{n+1-\theta}=\frac{1-\theta}{\theta}y^{n+\theta}+\frac{2\theta-1}{\theta}y^n,$$

$$3.\quad \frac{y^{n+1}(x)-y^{n+1-\theta}(x)}{\theta\Delta t^n}=f\left(y^{n+1}(x),\frac{y^{n+1}(x)-y^{n+1-\theta}(x)}{\theta\Delta t^n}\right).$$

3.1.1.2 Space discretization. The domain is approximated with a polygonal boundary and discretized by regular quadrilaterals. The problem is solved on three different meshes with 40×10, 60×15 and 80×20 elements. Pressure p / velocity $\mathbf{v}$ / parts of the stress $\mathbf{B}_{\kappa_{p_1(t)}}$ and $\mathbf{B}_{\kappa_{p_2(t)}}$ are approximated by $\mathrm{P}_1^{\mathrm{disc}}$ / Q_2 / Q_2 elements[1].

We utilize a fully coupled monolithic finite element approach that treats all the numerical variables simultaneously. At each time level the standard Galerkin method is used, the obtained set of non-linear algebraic equations is solved by the Newton method. The set of linear equations in every iteration of the Newton method is solved by the direct solver UMFPACK Davis (2004). The whole implementation is based on the code developed by Hron (2001) and used within the context of viscoelastic flow simulations (for Oldroyd and Maxwell model) in Damanik *et al.* (2010) and within the context of fluid-structure interaction problems (where the ALE formulation is essential as well) in Razzaq *et al.* (2012).

The angular velocity ω described by (6) changes in jumps. Instead of jumps we increase ω from zero to the desired value 0.5 rad s^{-1}, or decrease to zero smoothly on the time scale $t_1 = 0.001$s. It turns out that the result does not depend on t_1 if it is small enough. In fact, in the experiment the asphalt binder did not start/stop rotating immediately and so this approximation is very realistic.

[1] Q_2 stands for a continuous biquadratic element, $\mathrm{P}_1^{\mathrm{disc}}$ for a discontinuous bilinear element.

No adaptive time step was used, it was given apriori, the lowest time step was used when the rotating started/stopped and was of the order 10^{-5}s, the largest time step was of the order 10^{-3}s (two different sets of time steps were used). We have checked, that the results are independent of the mesh, time step size and used time scheme.

We present here the result obtained with the three-step θ time scheme and the mesh containing 1600 elements. The number of degrees of freedoms was 103 815 that is approximately 65 DOFs per one element (the set of 16 PDEs had to be solved at once using a monolithic solver).

We found out that the assumptions (7) made in deriving the ODE system were correct because it turns that the velocity magnitude in the rz direction was of the order 10^{-13} m/s, i.e. 10 orders of magnitude lower than in the ϕ direction. In the Figure 3 the snapshots of the full simulation at times $t = 0.025\text{s}, 0.5\text{s}, 0.6\text{s}, 2.0\text{s}$ are presented. It can be seen that at the beginning at $t = 0.025$s when it already rotates with the full speed the clockwise vortex is created and it remains there upto $t = 0.5$s when the rotation starts to stop. After the rotation stops, the velocity in rz direction decreases, and around $t = 0.6$s the counter-clockwise vortex is created and with the increasing time the velocity decreases. The velocity in the ϕ direction almost does not differ from the value $\omega rz/h$.

We also verified that the torque M and the normal force F on the upper plate computed in the full simulation by

$$M = \int_{\Gamma_U} rT_{\phi z}\,\mathrm{d}S = 2\pi \int_0^R r^2 T_{\phi z}\,\mathrm{d}r, \tag{19}$$

$$F = \int_{\Gamma_U} T_{zz}\,\mathrm{d}S = 2\pi \int_0^R rT_{zz}\,\mathrm{d}r. \tag{20}$$

is the same as the torque and the normal force obtained by Málek *et al.* (2014), see Figure 2.

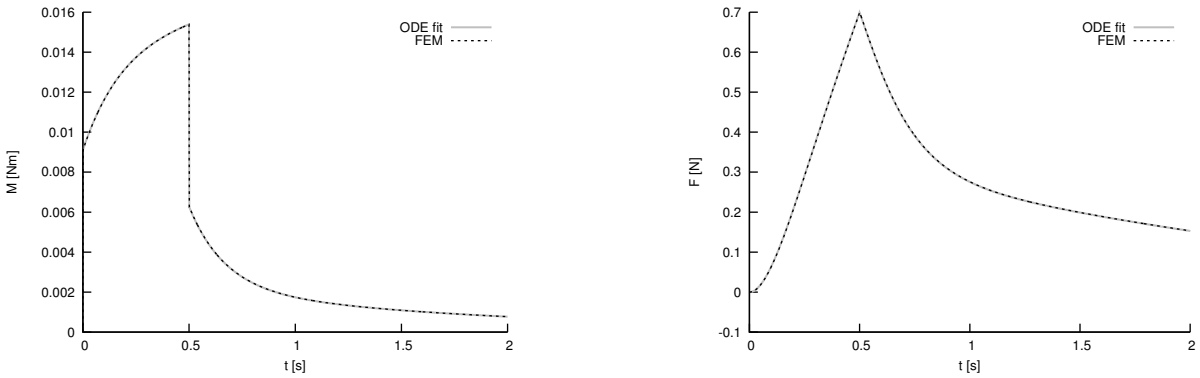

Figure 2. Comparison of the torque (left) and the normal force (right) obtained by FEM and by ODE fit by Málek *et al.* (2014).

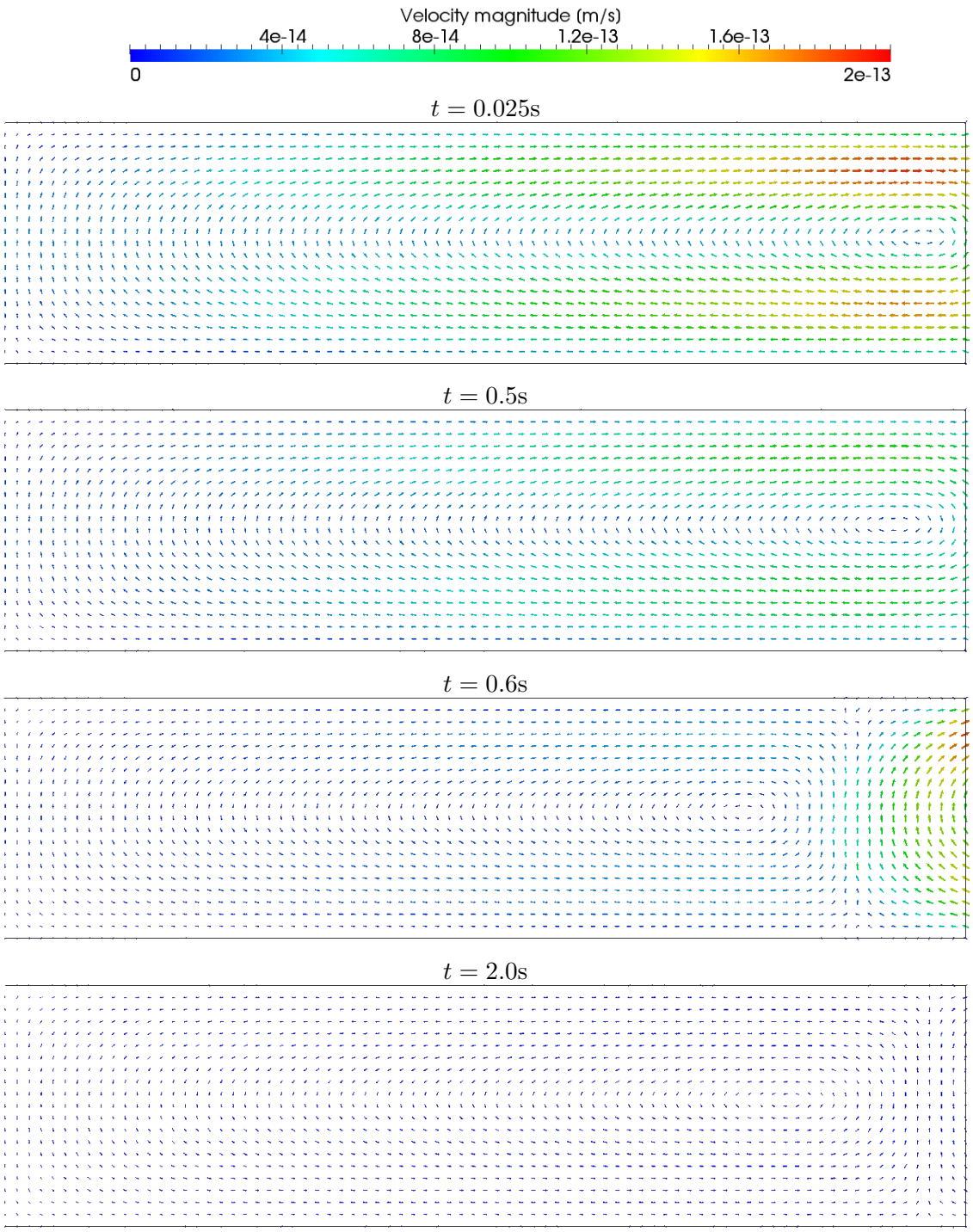

Figure 3. Snapshots of the full simulation of the experiment performed by Narayan et al. (2012).

3.2 *Simulations in time varying domains*

In this section we solve the more challenging problem of flows when the boundary is deforming. Since we are using a robust Finite element code with a monolithic non-linear solver we decided to transform the equations describing the non-linear Burgers model (1) from Eulerian description where the domain deforms into a description with a fixed domain. In order to do this we add a new variable associated with the deformation of the mesh $\hat{\mathbf{u}}$. The mapping $\hat{\varphi}$ maps fixed domain Ω_χ into the deforming domain Ω_x, see Figure 4.

There are two popular ways how this transformation is made. First, the fixed domain corre-

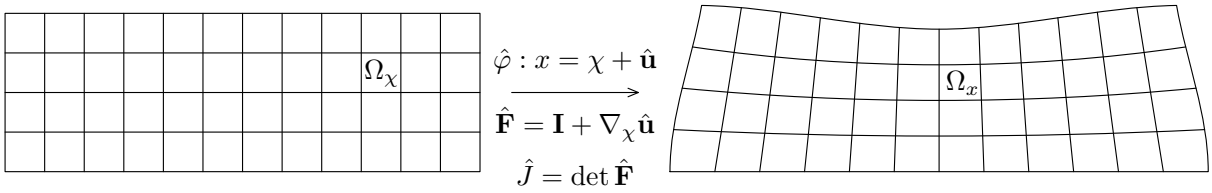

Figure 4. Deformation of the domain.

sponds to the Lagrangian description where all points in the domain are material points and $\hat{\mathbf{u}}$ is the physical deformation. However, some problems, like corruption of the virtual mesh, are connected with this approach. Second, the so-called Arbitrary Lagrangian-Eulerian (ALE) formulation where deformation $\hat{\mathbf{u}}$ is arbitrary with the restriction that the deformation is physical on the boundary of the domain. We present the application of ALE transformations for the non-linear version of the Burgers model (1), and it is done in the same way as that carried out by Hron *et al.* (2014).

3.3 *Arbitrary Lagrangian-Eulerian formulation*

We identify the computational mesh with the new domain Ω_χ (see Figure 5), where $\hat{\varphi}$ maps Ω_χ into Ω_x by

$$\hat{\varphi} : \chi \to x := \chi + \hat{\mathbf{u}}, \tag{21}$$

where $\hat{\mathbf{u}}$ is an arbitrary deformation (i.e. the deformation of the mesh). If the time derivative of $\hat{\mathbf{u}}$ is equal to the velocity $\mathbf{v}$ then all points would be the material points, $\Omega_\chi = \Omega_X$ and we would obtain the Lagrange formulation. Instead of this we only require that the material points on the boundary $\partial\Omega_\chi$, inside the domain Ω_χ need to have a unique solution for $\hat{\mathbf{u}}$, for simplicity we use a Laplace equation, i.e.

$$\hat{\mathbf{u}} = \begin{cases} \dfrac{\partial \hat{\mathbf{u}}}{\partial t} = \mathbf{v} \ \text{ on } \partial\Omega_\chi \\ -\Delta_\chi \hat{\mathbf{u}} = 0 \text{ inside } \Omega_\chi. \end{cases} \tag{22}$$

We define the deformation gradient and its Jacobian by

$$\hat{\mathbf{F}} = \frac{\partial \hat{\varphi}}{\partial \chi} = \mathbf{I} + \nabla_\chi \hat{\mathbf{u}}, \quad \hat{J} = \det \hat{\mathbf{F}}. \tag{23}$$

The weak formulation (12) is transformed from Ω_x to Ω_χ in the following way. The velocity gradient transforms as

$$\nabla_\chi \mathbf{v} = \frac{\partial \mathbf{v}(\hat{\varphi}(\chi,t),t)}{\partial \chi} = \frac{\partial \mathbf{v}}{\partial x}\frac{\partial \hat{\varphi}}{\partial \chi} = (\nabla_x \mathbf{v})\hat{\mathbf{F}} \quad \Rightarrow \quad \nabla_x \mathbf{v} = (\nabla_\chi \mathbf{v})\hat{\mathbf{F}}^{-1}. \tag{24}$$

The transformation of the material time derivative is more difficult, first we compute

$$\left.\frac{\partial \alpha}{\partial t}\right|_\chi = \left.\frac{\mathrm{d}\alpha(\hat{\varphi}(\chi,t),t)}{\mathrm{d}t}\right|_\chi = \left.\frac{\partial \alpha}{\partial t}\right|_x + \left.\frac{\partial \alpha}{\partial x}\frac{\partial \hat{\varphi}}{\partial t}\right|_\chi = \left.\frac{\partial \alpha}{\partial t}\right|_x + \frac{\partial \hat{\mathbf{u}}}{\partial t} \cdot \nabla_x \alpha. \tag{25}$$

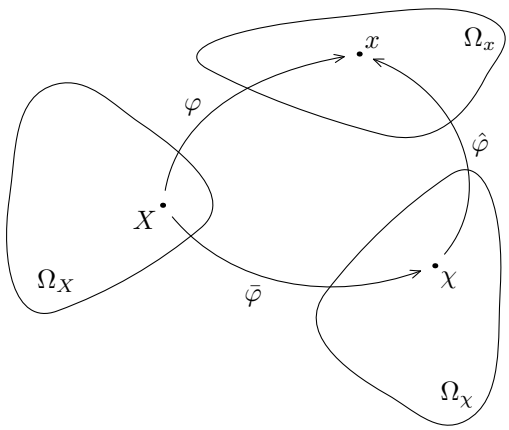

Figure 5. ALE formulation.

Using (25) we obtain

$$\begin{aligned}\frac{\partial \alpha}{\partial t}\Big|_x + \mathbf{v}\cdot\nabla_x\alpha &= \frac{\partial \alpha}{\partial t}\Big|_\chi + \left(\mathbf{v} - \frac{\partial \hat{\mathbf{u}}}{\partial t}\right)\cdot\nabla_x\alpha \\ &= \frac{\partial \alpha}{\partial t}\Big|_\chi + \left(\mathbf{v} - \frac{\partial \hat{\mathbf{u}}}{\partial t}\right)\cdot(\nabla_\chi\alpha)\hat{\mathbf{F}}^{-1} \\ &= \frac{\partial \alpha}{\partial t}\Big|_\chi + \left(\hat{\mathbf{F}}^{-1}\left(\mathbf{v} - \frac{\partial \hat{\mathbf{u}}}{\partial t}\right)\right)\cdot\nabla_\chi\alpha. \end{aligned} \tag{26}$$

Using (24), (26), the integral substitution theorem and the Piola identity we transform the weak formulation (12) to

$$\int_{\Omega_\chi} \hat{J}\,\mathrm{tr}\left((\nabla_\chi\mathbf{v})\hat{\mathbf{F}}^{-1}\right) q\,\mathrm{d}\chi = 0, \tag{27a}$$

$$\int_{\Omega_\chi} \hat{J}\rho\left[\frac{\partial \mathbf{v}}{\partial t} + (\nabla_\chi\mathbf{v})\left(\hat{\mathbf{F}}^{-1}\left(\mathbf{v} - \frac{\partial \hat{\mathbf{u}}}{\partial t}\right)\right)\right]\cdot\mathbf{q}\,\mathrm{d}\chi - \int_{\Omega_\chi}\mathrm{div}_\chi\left(\hat{J}\hat{\mathbf{T}}\hat{\mathbf{F}}^{-T}\right)\cdot\mathbf{q}\,\mathrm{d}\chi = 0, \tag{27b}$$

$$\hat{\mathbf{T}} = -p\mathbf{I} + \nu\left((\nabla_\chi\mathbf{v})\hat{\mathbf{F}}^{-1} + \hat{\mathbf{F}}^{-\mathrm{T}}(\nabla_\chi\mathbf{v})^{\mathrm{T}}\right) + \mu_1\mathbf{B}^d_{\kappa_{p_1(t)}} + \mu_2\mathbf{B}^d_{\kappa_{p_2(t)}}, \tag{27c}$$

$$\begin{aligned}\int_{\Omega_\chi}\hat{J}\Bigg[&\frac{\partial \mathbf{B}_{\kappa_{p_1(t)}}}{\partial t} + (\nabla_\chi\mathbf{B}_{\kappa_{p_1(t)}})\left(\hat{\mathbf{F}}^{-1}\left(\mathbf{v} - \frac{\partial \hat{\mathbf{u}}}{\partial t}\right)\right) \\ &-(\nabla_\chi\mathbf{v})\hat{\mathbf{F}}^{-1}\mathbf{B}_{\kappa_{p_1(t)}} - \mathbf{B}_{\kappa_{p_1(t)}}\hat{\mathbf{F}}^{-\mathrm{T}}(\nabla_\chi\mathbf{v})^{\mathrm{T}} + \frac{1}{\tau_1}\mathbf{B}_{\kappa_{p_1(t)}}\mathbf{B}^d_{\kappa_{p_1(t)}}\Bigg]\cdot\mathbf{Q}_1\,\mathrm{d}\chi = 0,\end{aligned} \tag{27d}$$

$$\begin{aligned}\int_{\Omega_\chi}\hat{J}\Bigg[&\frac{\partial \mathbf{B}_{\kappa_{p_2(t)}}}{\partial t} + (\nabla_\chi\mathbf{B}_{\kappa_{p_2(t)}})\left(\hat{\mathbf{F}}^{-1}\left(\mathbf{v} - \frac{\partial \hat{\mathbf{u}}}{\partial t}\right)\right) \\ &-(\nabla_\chi\mathbf{v})\hat{\mathbf{F}}^{-1}\mathbf{B}_{\kappa_{p_2(t)}} - \mathbf{B}_{\kappa_{p_2(t)}}\hat{\mathbf{F}}^{-\mathrm{T}}(\nabla_\chi\mathbf{v})^{\mathrm{T}} + \frac{1}{\tau_2}\mathbf{B}_{\kappa_{p_2(t)}}\mathbf{B}^d_{\kappa_{p_2(t)}}\Bigg]\cdot\mathbf{Q}_2\,\mathrm{d}\chi = 0.\end{aligned} \tag{27e}$$

This set of equations is closed with the equation (22) written in the weak formulation as

$$\int_{\Omega_\chi}\nabla_\chi\hat{\mathbf{u}}\cdot\nabla_\chi\mathbf{t}\,\mathrm{d}\chi = 0. \tag{28}$$

3.3.1 Finite element method for ALE formulation

In the rest of the paper we compute four problems that differ only in the domain and the boundary conditions. Finite element method, as described in 3.1.1, is based on the weak formulation consisting of (27) and (28) with one difference in the balance of linear momentum where the divergence theorem is used

$$\int_{\Omega_\chi} \hat{J}\rho \left[\frac{\partial \mathbf{v}}{\partial t} + (\nabla_\chi \mathbf{v}) \left(\hat{\mathbf{F}}^{-1} \left(\mathbf{v} - \frac{\partial \hat{\mathbf{u}}}{\partial t} \right) \right) \right] \cdot \mathbf{q} \, \mathrm{d}\chi = - \int_{\Omega_\chi} \hat{J}\hat{\mathbf{T}}\hat{\mathbf{F}}^{-T} \cdot \nabla_\chi \mathbf{q} \, \mathrm{d}\chi + \int_{\partial\Omega_\chi} \left(\hat{J}\hat{\mathbf{T}}\hat{\mathbf{F}}^{-T} \right) \mathbf{n}_\chi \cdot \mathbf{q} \, \mathrm{d}S_\chi, \tag{29}$$

where $\mathbf{n}_\chi$ is the outer unit normal vector in the space Ω_χ. The last term in (29) is used for prescribing the Neumann boundary condition. Specifically, we prescribe $\left(\hat{J}\hat{\mathbf{T}}\hat{\mathbf{F}}^{-T} \right) \mathbf{n}_\chi$ as a force acting on the part of boundary $\partial\Omega_\chi$. This means that we prescribe a vector whose components are perpendicular/parallel with the normal vector in the actual configuration and so we can easily push the material perpendicularly to the boundary. For simplicity of notation later in the text when we write about the boundary conditions instead of writing the component $(\hat{J}\hat{\mathbf{T}}\hat{\mathbf{F}}^{-T})_{ij}$ it will be written the component T_{ij}.

In all problems the material is at rest at $t = 0$, the initial conditions are given by (4) and $\hat{\mathbf{u}} = \mathbf{0}$. The boundary conditions are different in each problem, but all problems have these common boundary conditions: for all problems no boundary condition is used for $\mathbf{B}_{\kappa_{p_1(t)}}$ and $\mathbf{B}_{\kappa_{p_2(t)}}$ and the Dirichlet condition is used for the deformation $\hat{\mathbf{u}}$

$$\frac{\partial \hat{\mathbf{u}}}{\partial t} = \mathbf{v} \text{ on } \partial\Omega_\chi.$$

As mentioned in the subsubsection 3.1.1 the domain Ω_χ is discretized by regular quadrilaterals. The mesh that is used is depicted in the Figures describing each problem, all meshes are refined near the boundary. Pressure p/deformation $\hat{\mathbf{u}}$/velocity $\mathbf{v}$/parts of the stress $\mathbf{B}_{\kappa_{p_1(t)}}$ and $\mathbf{B}_{\kappa_{p_2(t)}}$ are approximated by $\mathrm{P}_1^{\mathrm{disc}}/\mathrm{Q}_2/\mathrm{Q}_2/\mathrm{Q}_2$ elements. The time derivatives are discretized by the implicit Glowinski three-step time scheme with a constant time step $\Delta t = 0.01$s for all problems.

3.4 *Problem 1 – Response of the model to a suddenly applied normal load for a short duration.*

In this problem let us consider a rectangular piece of material, see Figure 6. Its width is 3m, the height is 1m.[1] The material rests on the ground where it can fully slip in the x-direction, but it is not allowed to move in the y-direction. All other sides of the rectangle can move freely. We ignore the effect of gravity. At $t = 0$ the material is at rest. Suddenly at time $t = 0$ the body is pushed at the top by a constant normal stress $T_{yy} = -5$ kPa. This stress acts till the time $t = 0.5$s, and then it suddenly ceases to exist. We observe how the boundary continues to deform after the applied traction ceases.

The boundary conditions are:

Bottom Dirichlet: $v_y = 0$, Neumann: $T_{xy} = 0$
Top and sides Neumann: $\mathbf{Tn} = \mathbf{0}$, during the pressing $T_{yy} = -5$ kPa on a part of the boundary.

We solve this problem with the model (1) using the real material parameters, see Table 1.

Every set of material parameters is numbered by $N = 1, \ldots, 4$. For the material parameters $N = 2, 3, 4$ the model (1) is equivalent to model with one natural configuration (5) with $\mu = \mu_1 + \mu_2$ and $\tau = \tau_1 = \tau_2$. Density $\rho = 1000$ kg/m^3 is used in all cases. All problems are computed on a fixed mesh 60×20 (locally refined near the boundary) with constant time step $\Delta t = 0.01$ and three step θ time scheme.

[1] We use a thick layer of viscoelastic material in order to capture the elastic response. Later, we shall use much thinner domains as the application we have in mind are pavements which are usually modeled as rate type viscoelastic fluids, which

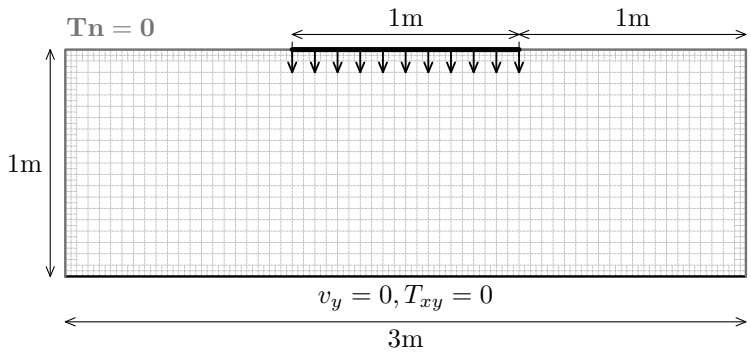

Figure 6. Pressing of the rectangular piece of viscoelastic material.

N	ν [Pa s]	τ_1 [s]	τ_2 [s]	μ_1 [kPa]	μ_2 [kPa]
1	100.0	0.2	2.0	10.0	5.0
2	100.0	0.2	0.2	10.0	5.0
3	100.0	0.8	0.8	10.0	5.0
4	100.0	2.0	2.0	10.0	5.0

Table 2. Material parameters used in the simulation of rectangle compression.

In the first problem we show how the viscoelastic model (1) behaves. Our aim is to describe the response of the model in a nontrivial geometry and show the influence of the relaxation times τ_1 and τ_2 on the solution.

For $N = 1$ all the material parameters are different and we are hence using the full model (1), the elastic moduli μ_1 and μ_2 in model (1) determine the weights corresponding to the relaxation times τ_1 and τ_2. The more μ_1 is higher than μ_2, the more the material behaves as a material with the relaxation time τ_1 as the dominant relaxation time. That is why we also use material parameters where relaxation times $\tau = \tau_1 = \tau_2 = 0.8$s which is a weighted average of the material parameters $N = 1$ in the sense

$$\tau = \frac{\mu_1\tau_1 + \mu_2\tau_2}{\mu_1 + \mu_2}.$$

We found that the steady solution of the model with this averaged relaxation time and the model with material parameters for $N = 1$ is almost the same.

We carried out the full simulations for four materials described by non-linear model (1) listed in Table 2 and we have a fully dynamic movie of the response of each of these materials from which we have picked five snapshots of the deformation of the top side (lateral sides are not depicted). Figure 7 depicts how the y-component of the deformation at the center line depends on time. This problem was also computed using the real material parameters given by Table 1 with the normal stress equal to 100 kPa, the result is also depicted in Figure 7 and it can be seen that the behavior is mostly viscous.

Vertical lines in the graph denote the times when the snapshots are captured: 0.53s (minimum for material $N = 1$), 0.7s, 0.94s (maximum for material $N = 3$ and $N = 4$) and 1.16s (maximum for $N = 1$). The snapshots are depicted in Figure 8.

The body described by $N = 4$ exhibits both elasticity and damping, and with the material $N = 3$ it exhibits similar behavior but with less elasticity (or with more damping). The material $N = 2$ behaves mostly like a viscous fluid, on pressing the top surface there is only one small wave and the material remains deformed. The most interesting response characteristics are exhibited

are much wider than thick.

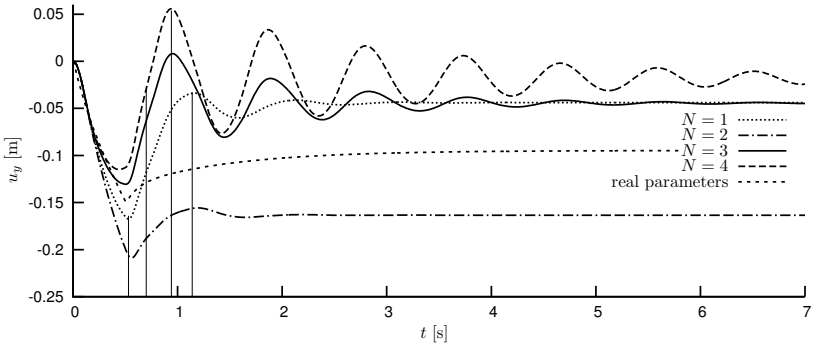

Figure 7. Dependence of the deformation u_y of the center point at the top surface with time t.

by the full model (1) with the material $N = 1$, in that the displacement after an initial oscillation remains essentially constant.

All the simulations were carried out upto the time $t = 40.0$s when even the viscoelastic fluid with the greatest elastic response ceases to deform further.

The snapshots in Figure 8 show that in the most elastic case the shape of the surface at its maximum is almost concave compared to the other material parameters. Further it can be seen that at time 40.0s when all materials cease to deform, the deformations of the full model $N = 1$ and for material $N = 3$ are almost the same (dotted line merges the dot-and-dashed line), that is, asymptotically in time both these models have the same response, though their transient response is different.

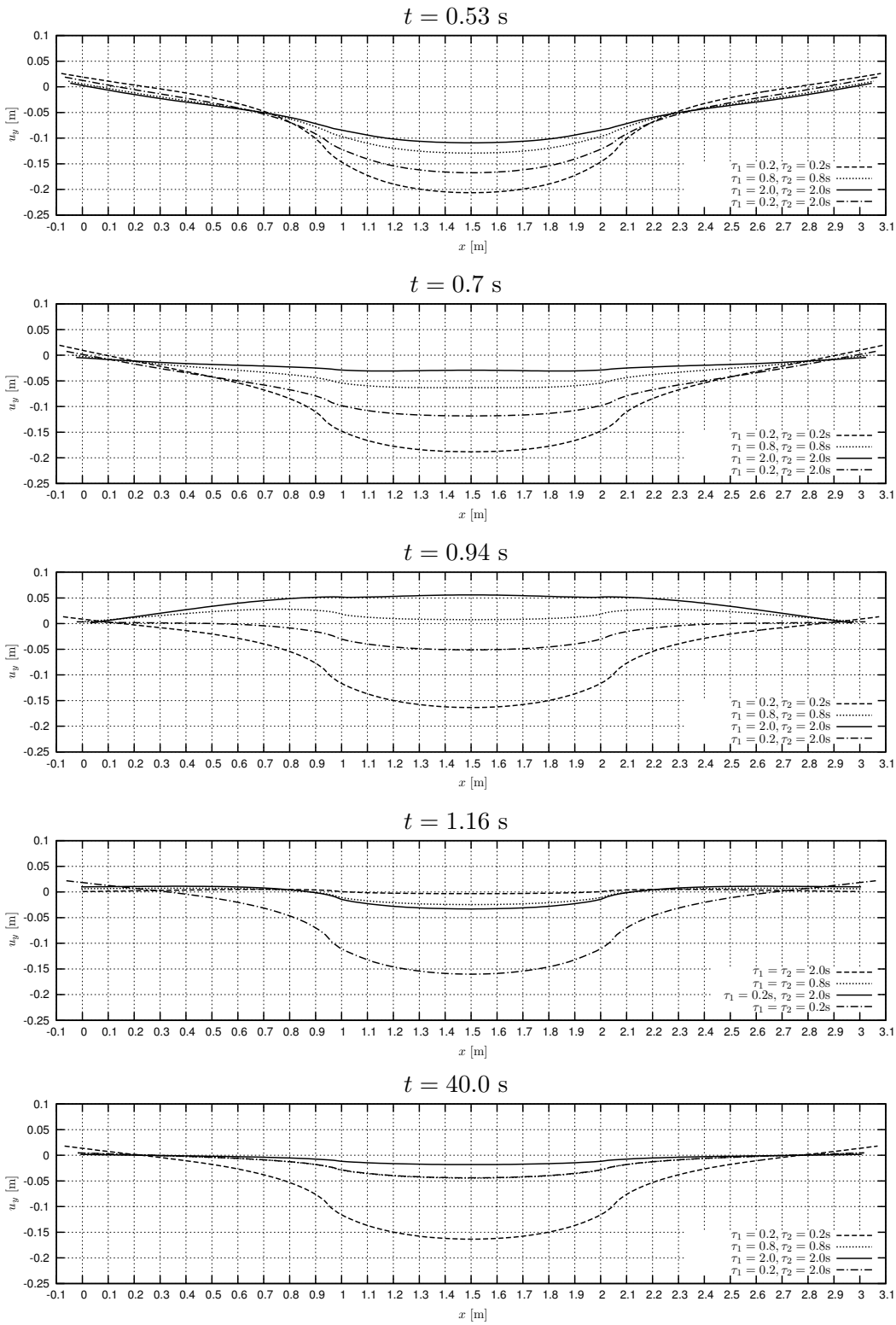

Figure 8. Snapshots of the top side at five different times.

3.5 *Problem 2 – Application of the same constant total force over differing areas (i.e. different normal boundary stresses) for a fixed duration of time.*

Next, let us consider a rectangular piece of material, its width being 3m and its height 0.5m. Model (1) with the real material parameters given by Table 1 is used together with density $\rho = 1200\text{kg/m}^3$. At the bottom the material can fully slip in the x-direction, but it can not move in the y-direction. The material can not flow throw the lateral sides but it can fully slip in the y-direction. It can freely move on the top.

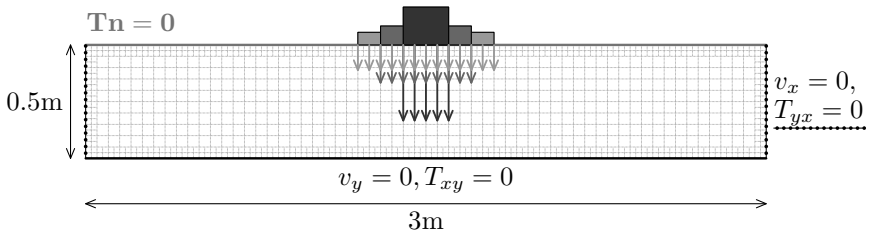

Figure 9. Application of constant force on different area.

The top surface is pressed in the middle (see Figure 9) from the time $t = 0$ till $t = 0.5$ s with a constant force $F = 50$ kN on three different areas of the length l: 60cm, 40cm and 20cm, using three different normal stresses $T_{yy} = -F/l$, see Figure 9. After $t = 0.5$ s the force is released and the material is allowed to relax.

The boundary conditions are the following:

Bottom Dirichlet: $v_y = 0$, Neumann: $T_{xy} = 0$
Lateral sides Dirichlet: $v_x = 0$, Neumann: $T_{yx} = 0$
Bottom corners : Dirichlet: $v_x = v_y = 0$
Top Neumann: $\mathbf{Tn} = \mathbf{0}$, during the pressing $T_{yy} = -(F/l)$ Pa on three different parts of the boundary, F=50 kN.

In the Figure 10 the deformation of the top surface for three different normal stresses and three different areas is depicted. Each deformation is drawn with one color, snapped at two different times. The end of the compression $t = 0.5$ s (dotted line) and at $t = 10$ s (solid line) when the flow is settled down are indicated in the figure.

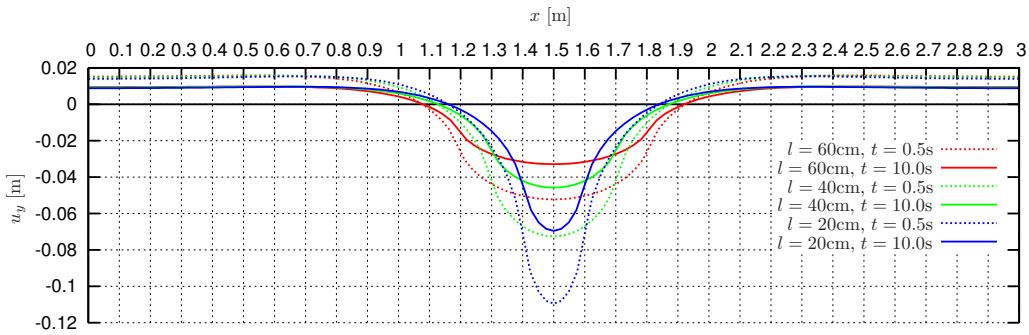

Figure 10. The deformations of the top surface for three different normal stresses and areas at two different times: Area of the length $l = 60$cm (red line), $l = 40$cm (green line) and $l = 20$cm is pressed with the normal stress $T_{yy} = -(F/l)$ Pa with $F = 50$ kN. Every color is depicted at the end of the application of the force at $t = 0.5$ s (dotted line) and at $t = 10$ s (solid line) when the top side is settled down.

3.6 *Problem 3 – The problem of rutting.*

The next problem that we study is relevant to the problem of rutting that is observed on roadways due to the constant motion of heavy transportation vehicles. The tires of these vehicles repeatedly go over a small part of the roadway and one can clearly observe the depression that is made due to such a motion on the roadway.

The problem is computed with the real material parameters given by Table 1. Let us consider a rectangular piece of roadway as given in Figure 11. The width is 3m, the height is 0.2m. The vehicles are assumed to move along the z-direction and the tires of the vehicles apply a load on the roadway as shown. We have assumed that the tires are 0.25m wide. At the bottom surface we will assume that the material can fully slip in the x-direction, but it can not move in the y-direction. The material can not flow through the lateral sides but it can fully slip in the y-direction. It can freely move on the top.

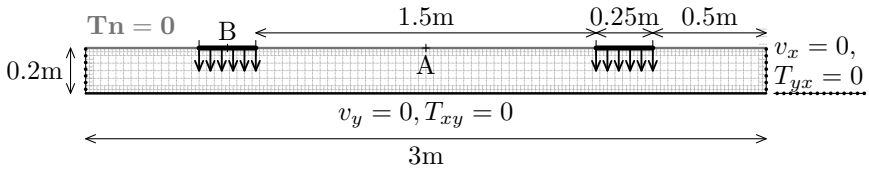

Figure 11. Problem of rutting in the road.

The material is pushed by constant normal stress $T_{yy} = -20$ kPa due to the contact of the tires with the roadway as depicted in Figure 11. Let us assume that there are twenty passes of the vehicles over a particular region and that the tire of vehicle stays in contact with the roadway at that location for 0.5s. Let us also assume the time interval between two vehicles approaching the same location is 3.5s. Thus, the body is given 3.5s to relax. Let us suppose that the material is pressed between the times t_1^k and t_2^k, where $t_1^k = (4.0k)$s and $t_2^k = (0.5 + 4.0k)$s for $k = 0, \ldots, 19$.

The boundary conditions are:

Bottom surface Dirichlet: $v_y = 0$, Neumann: $T_{xy} = 0$
Lateral sides Dirichlet: $v_x = 0$, Neumann: $T_{yx} = 0$
Bottom corners Dirichlet: $v_x = v_y = 0$
Top surface Neumann: $\mathbf{Tn} = \mathbf{0}$, during the pressing $T_{yy} = -20$ kPa on a part of the boundary.

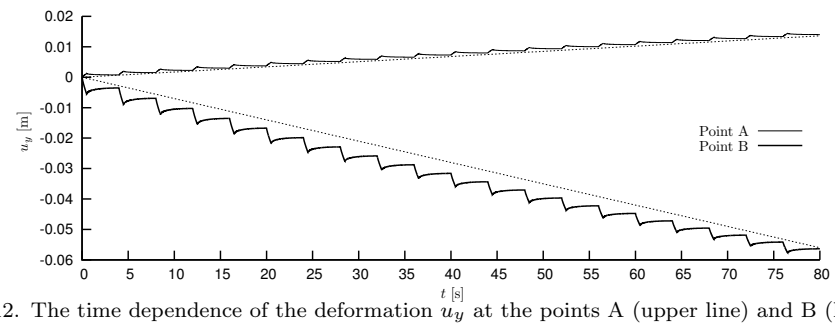

Figure 12. The time dependence of the deformation u_y at the points A (upper line) and B (lower line).

The time dependence of the deformation u_y of two points A and B on the top surface (see Figure 11) is depicted in Figure 12. We observe that the deformation u_y is non-linear with time t, for the point B this can be seen clearly (compare with the dotted linear line), in case of point A the deformation is also non-linear but this can not be seen in the presented scale. The non-linear deformation is caused because the non-linear model (1) was used and it is also the result of the boundary condition that is assumed to hold at the bottom.

In Figure 13 we depict the result of compressing a roadway. For the purpose of illustration, only the evolution of the deformation of the top surface with time for their first, the tenth and the twentieth compression is portrayed. Each compression is drawn in a different color. The beginning of the compression is denoted by a dotted line and the end by a dashed line and the deformation four seconds after the beginning of the compression by a solid line. It can be seen that the material is most deformed during the first compression, and least deformed during the last twentieth compression. The full movie of rutting is available in the online version, at ...

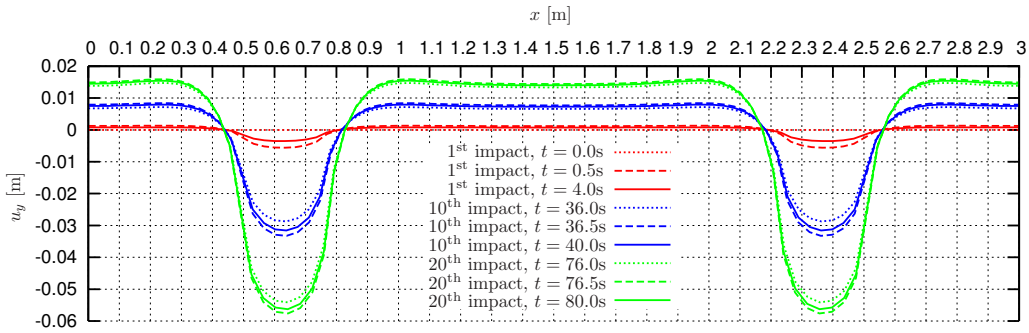

Figure 13. Time snapshots of the top side depicting the first (red line), the tenth (blue line) and the twentieth (green line) application of force. Corresponding to these applications of compressive loads at the top surface the beginning of the application by a dotted line, the end of the application by a dashed line and the deformation four seconds after the beginning of the application by a solid line.

3.7 *Problem 4 – Rolling of the asphalt.*

The last problem is the rolling of the asphalt on the runway. Let us consider the rectangular piece of material, the width is 3m, the height is 0.5m. The problem is computed with the model (1) and the real material parameters given by the Table 1 are used with the density $\rho = 1200$ kg/m^3. The problem is depicted in the Figure 14. The material is on the ground where it can fully slip in the x-direction, but it can not move in the y-direction. All other sides of the rectangle can freely move.

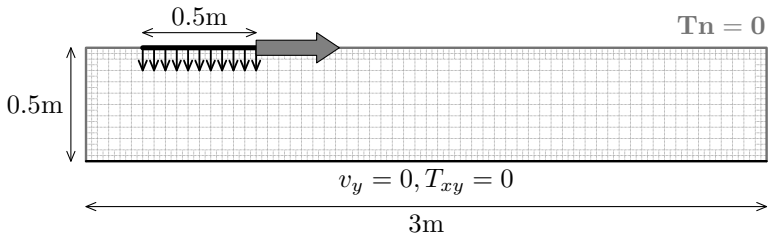

Figure 14. Rolling of the asphalt.

At the beginning the material is in rest and does not move. Suddenly at time $t = 0$ it is pushed at the top with a constant normal stress $T_{yy} = -50$ kPa. The force is applied on the constant area $l = 50$cm corresponding to the weight $m = 2\,500$ kg and this area moves with the velocity 40 cm/s from the left to the right and then back to the left, i.e. the asphalt is rolled forward and back. In the Figure 15 the location of the area borders is depicted with respect to time t. The force is released at $t = 10.4$ s and the material is let to relax.

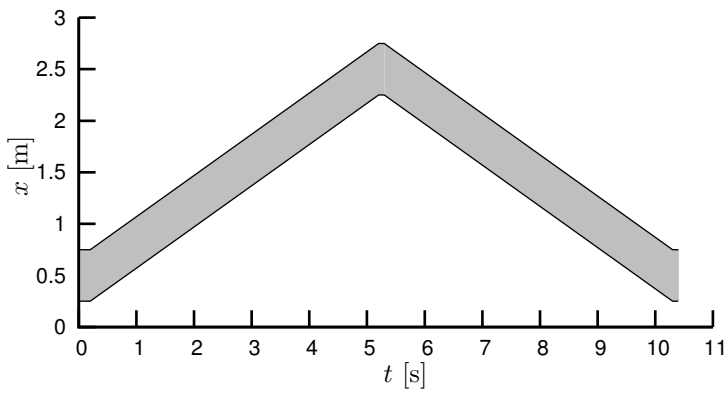

Figure 15. The location of the area where the force is applied with respect to time.

The boundary conditions are:

Bottom Dirichlet: $v_y = 0$, Neumann: $T_{xy} = 0$

Top and sides Neumann: $\mathbf{Tn} = \mathbf{0}$, during the pressing $T_{yy} = -50$ kPa on the moving part of the boundary.

In the Figure 16 there are five snapshots of the whole simulation. It can be seen how the asphalt is rolled into the sides, the snapshot at $t = 6.5$ shows how the roller pushes the asphalt ahead. The last two snapshots show the relaxation of the asphalt due to the elastic part of response. The full movie of rolling is available in the online version, at ...

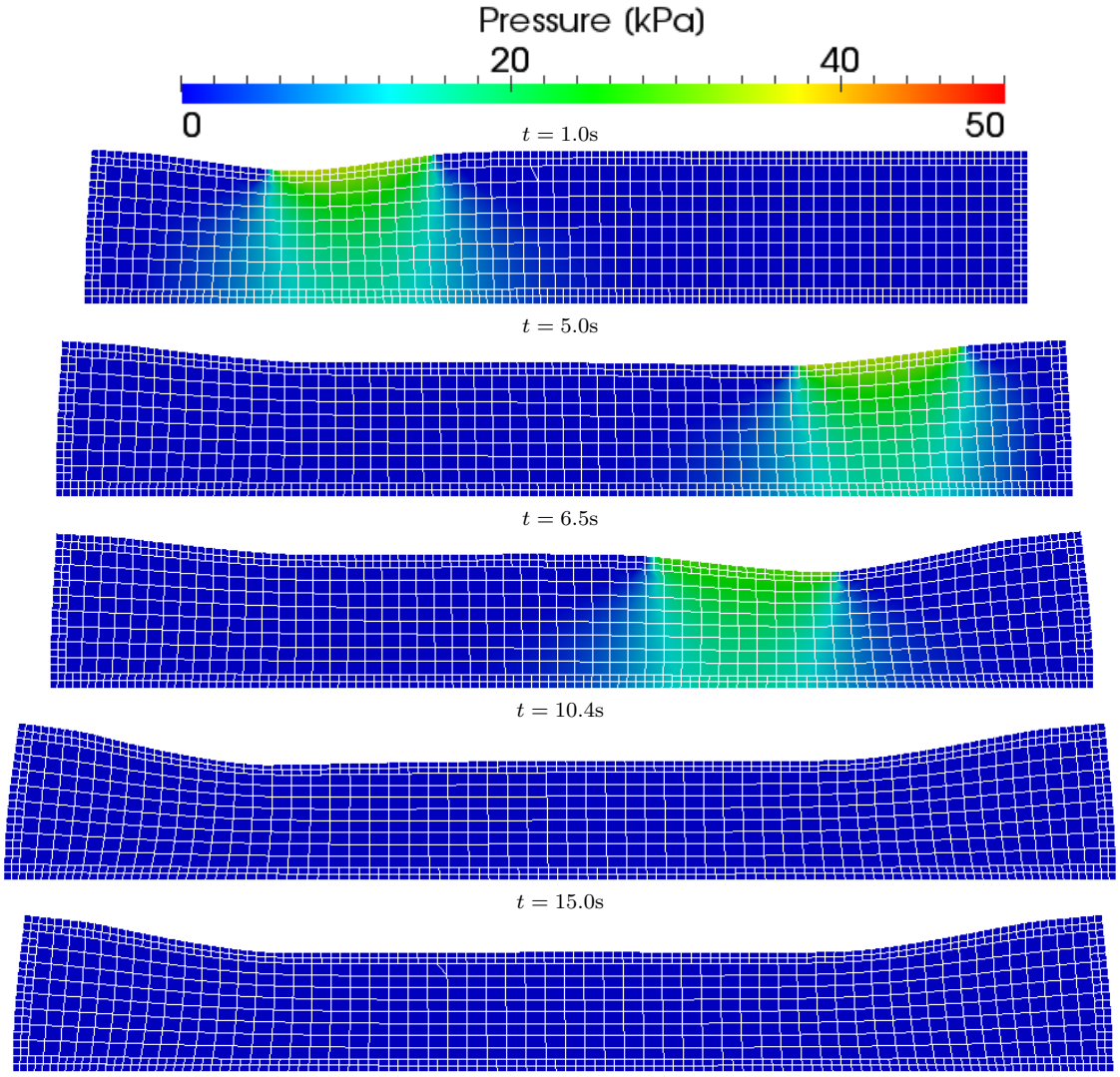

Figure 16. Snapshots of the rolling of the asphalt.

4. Conclusion

We have used the finite element method to simulate complex flow of the viscoelastic rate type fluid that has been corroborated against experiments on asphalt binder. The asphalt binder has two relaxation times associated with it, one that describes the relaxation of shear stresses and the other the relaxation of normal stresses. This model was developed by Málek *et al.* (2014) and it was shown there that this model is a non-linear version of a standard viscoelastic Burgers model. Málek *et al.* (2014) obtained the material parameters for the model (1) by comparing its predictions against the experiment on asphalt binders under the assumption of the form of a special form for velocity field. We computed the full simulation of the experiment with given material parameters and obtained the same result for the torque and the normal force.

We formulated the model (1) into an ALE description and used it to compute four simulations of the problems with a deforming boundary. The problems that were considered have relevance to important problems in transportation technology such as that of rutting and compaction by rolling.

5. Acknowledgements

J. Málek and K. Tůma acknowledge the support of the ERC-CZ project LL1202 financed by MŠMT (Ministry of Education). K. R. Rajagopal thanks the Office of Naval Research and the National Science Foundation for its support.

References

Damanik, H., *et al.*, 2010. A monolithic FEM approach for the log-conformation reformulation (LCR) of viscoelastic flow problems. *Journal of Non-Newtonian Fluid Mechanics*, 165 (1920), 1105 – 1113.

Davis, T.A., 2004. Algorithm 832: UMFPACK V4. 3—an unsymmetric-pattern multifrontal method. *ACM Transactions on Mathematical Software (TOMS)*, 30 (2), 196–199.

Glowinski, R., 1985. Viscous flow simulation by finite element methods and related numerical techniques. *In*: *Progress and supercomputing in computational fluid dynamics; Proceedings of US-Israel Workshop, Jerusalem, Israel, December 1984 (A86-46787 22-34)*., Vol. 1 Birkhaeuser Boston, 173–210.

Glowinski, R., 2003. Finite element methods for incompressible viscous flow. *In*: P. Ciarlet and J. Lions, eds. *Numerical Methods for Fluids (Part 3)*., Vol. 9 of *Handbook of Numerical Analysis* Elsevier, 3 – 1176.

Hron, J., 2001. Fluid structure interaction with applications in biomechanics. Thesis (PhD). Charles University.

Hron, J., Rajagopal, K.R., and Tůma, K., 2014. Flow of a Burgers fluid due to time varying loads on deforming boundaries. *Journal of Non-Newtonian Fluid Mechanics*.

Krishnan, J.M. and Narayan, A., 2007. Steady Shear Experiments on Ashpalt. [online] Internal Report [IIT, Madras, Chennai].

Krishnan, J.M. and Rajagopal, K.R., 2005. On the mechanical behavior of asphalt. *Mechanics of Materials*, 37 (11), 1085 – 1100.

Málek, J., Rajagopal, K.R., and Tůma, K., 2014. A thermodynamically compatible model for describing the response of asphalt binders. *International Journal of Pavement Engineering*.

Narayan, A., *et al.*, 2012. Nonlinear viscoelastic response of asphalt binders: An experimental study of the relaxation of torque and normal force in torsion. *Mechanics Research Communications*, 43 (0), 66 – 74.

Rajagopal, K.R. and Srinivasa, A.R., 2004. On the thermomechanics of materials that have multiple natural configurations Part I: Viscoelasticity and classical plasticity. *Zeitschrift Fur Angewandte Mathematik Und Physik*, 55, 861–893.

Razzaq, M., *et al.*, 2012. FEM multigrid techniques for fluidstructure interaction with application to hemodynamics. *Applied Numerical Mathematics*, 62 (9), 1156 – 1170 Numerical Analysis and Scientific Computation with Applications (NASCA) 2009.

Turek, S., *et al.*, 2006. Numerical study of a modified time-stepping θ-scheme for incompressible flow simulations. *Journal of Scientific Computing*, 28 (2-3), 533–547.